PAPER

Cite this: *Nanoscale Adv.*, 2025, **7**, 6941

Development of flexible piezoresistive pressure sensors *via* direct ink writing of MWCNT/PDMS nanocomposite inks: rheological and electromechanical characterization

Jashanpreet Singh Sidhu, [ID] * Aviral Misra [ID] and Arvind Bhardwaj [ID]

The integration of nanoscience and 3D printing has given rise to the emerging field of printable and flexible electronics. Direct ink writing (DIW) has transformed the field of 3D printing by using viscoelastic inks, ensuring design, intricacy, and flexibility. This study presents the fabrication of flexible piezoresistive pressure sensors using multiwalled carbon nanotubes (MWCNTs)/polydimethylsiloxane (PDMS) based conductive inks *via* the DIW method. Three ink formulations were prepared with MWCNT concentrations of 2 wt%, 4 wt%, and 6 wt% to investigate their rheological and printability characteristics. Rheological analysis revealed that MWCNT loading concentrations above 4 wt% impart shear-thinning behavior and solid-like viscoelastic properties essential for DIW printing. Among the formulations, the 6 wt% MWCNT/PDMS ink exhibited the best printability and structural integrity for porous woodpile architectures. Morphological analysis confirmed the dispersion of MWCNTs within the PDMS matrix, indicating an effective filler distribution and network formation throughout the composite. Mechanical testing demonstrated that 6 wt% MWCNT/PDMS exhibited a threefold increase in Young's modulus (3.61 MPa) and a higher tensile strength (2.44 MPa) compared to pristine PDMS, owing to effective stress transfer and nanotube reinforcement. Cyclic tensile fatigue tests confirmed the CNT-6 composite's mechanical stability and low stress softening at lower strains, underscoring its durability for flexible pressure sensor applications. The fabricated pressure sensor demonstrated a pronounced piezoresistive response with a high sensitivity of 0.047 kPa^{-1}, along with excellent repeatability and stability under both static and dynamic loading conditions, establishing its potential for precision pressure monitoring in flexible and wearable sensing applications.

1 Introduction

Flexible and stretchable electronics are crucial for various smart technologies, including robotics, prosthetics, wearable electronics, and energy-harvesting devices.[1] The burgeoning demand for smart wearable and healthcare technologies has resulted in notable progress in the development of flexible sensors for measuring purposes.[2,3] Soft and flexible pressure sensors have garnered significant interest due to their prospective use in electronic skin,[4] healthcare monitoring,[5] soft robotic systems,[6] *etc.* Comprehensive research has been conducted to investigate several facets of flexible sensors, including their material characteristics, fabrication techniques, and applications.[7,8] Various sensing mechanisms, such as piezoresistive, piezoelectric, capacitive, and triboelectric, have been employed in the development of flexible and soft pressure

sensors.[9] Among these, piezoresistive sensors are particularly attractive because of their simple structural design, cost-effective fabrication, straightforward signal acquisition, and high sensitivity.[10] Conventionally, piezoresistive sensors primarily rely on the geometrical deformation of the bulk sensing material under applied pressure, which often suffers from limited sensitivity and a narrow operational range.[11] An improved structural design, particularly the construction of porous microstructures, improves the functionality of pressure sensors.[12] Porous structures fabricated using soft conductive composites at millimeter and micrometer scales have been extensively used in pressure sensors owing to their ability to provide much higher strain levels than bulk solid alternatives.[13] Currently, micro- and macro-structured features in pressure sensors are mostly fabricated using techniques such as photolithography and sacrificial template methods, which are costly, highly complex, and time-intensive.[14,15] To resolve these challenges, it is essential to develop a straightforward, economical, and efficient approach for the fabrication of soft pressure

Department of Industrial and Production Engineering, Dr B R Ambedkar National Institute of Technology, Jalandhar-144008, India. E-mail: jashanpreetss.ip.21@nitj.ac.in

sensors featuring well-regulated microstructures that have optimal sensing capability.

Advancements in the field of additive manufacturing (AM) have allowed the manufacture of 3D printed components to provide the benefits of product customization, material waste reduction, and faster production.[16] This allows for greater design freedom, customization, and scalability than conventional manufacturing methods.[17] 3D printing constructs electrical devices incrementally and has significantly improved the controllability and tunability of device architectures. Among several 3D printing techniques, direct ink writing (DIW) is a notable technology that is especially advantageous for the fabrication of both micro- and macro-structures pressure sensors because of its simplicity, efficiency, and cost-effectiveness.[18,19] DIW is an extrusion-based technique that utilizes viscoelastic inks and a software-controlled bed with a syringe nozzle to print materials with tailored structures and compositions.[20] DIW accommodates a wide range of materials, including polymers, hydrogels, nanomaterials, ceramics, and emulsions. However, effective 3D-printing requires inks to exhibit shear-thinning behavior, a suitable yield stress, viscosity, and modulus to ensure printability and shape retention. Nanomaterials exhibit unique mechanical, chemical, and electronic properties, which can be attributed to their specific sizes and structures. Nanomaterials such as multi-walled carbon nanotubes (MWCNTs) have great potential for use in flexible sensors due to their low percolation threshold, high conductivity, and mechanical flexibility under bending and stretching.[21,22] Chen et al.[23] developed a soft pressure sensor through DIW of porous polyurethane foam substrates, subsequently dip-coated with CNT suspensions. Li et al.[24] successfully 3D printed stretchable capacitive sensors for tactile and electrochemical sensing using the DIW technique. Mena et al.[25] demonstrated the effect of MWCNT concentration on the electrical conductivity and fabricated wearable strain sensors based on polymer-reinforced MWCNT composites using solvent casting. Wang et al.[26] enhanced the mechanical properties of flexible circuits by inkjet printing with CNT-doped silver oxide ink. Elizabeth et al.[27] developed an MWCNT/polydimethylsiloxane (PDMS) composite sensor via a simple dispersion–freezing method for monitoring human flexion movements. Naeem et al.[28] enhanced the thermoelectric performance of flexible functionalized MWCNT films by fabricating them via vacuum filtration and optimizing their properties through hot-pressing at different temperatures. Singh et al.[29] fabricated serpentine and I-shaped flexible strain sensors by drop-casting a MWCNT/graphene composite onto a polymer substrate. Although nanomaterial-based flexible sensors have shown great potential, their performance is often constrained by structural limitations. Structural design is therefore a key strategy to enhance sensitivity, pressure range, and positive piezoresistive response. Engineered geometries such as micropyramids, domes, porous lattices, woodpile structures, and serpentine traces amplify strain concentration and modulate contact areas, thereby producing pronounced resistance variations and enhancing the sensitivity of flexible pressure sensors.[30–32] Owing to the high design freedom of extrusion-

based 3D printing, these architectures can be systematically optimized to achieve enhanced sensitivity and stable piezoresistive behavior. However, conventional fabrication methods are mostly restricted to two-dimensional structures with restricted complexity and versatility. To overcome these challenges, 3D-printable inks with tuned rheological properties were formulated for the single-step DIW of flexible pressure sensors exhibiting piezoresistive behavior.

This study presents a systematic approach for the one-step fabrication of flexible piezoresistive pressure sensors via DIW printing using MWCNT/PDMS-based viscoelastic inks. The development of the MWCNT/PDMS ink has been discussed in detail. MWCNT/PDMS inks with concentrations of 2 wt%, 4 wt%, and 6 wt% of MWCNTs were formulated to analyze their printability characteristic in DIW. The rheological properties of the MWCNT/PDMS inks were analyzed using a shear rate-controlled rotational test and oscillatory shear tests. The role of MWCNT concentrations on ink shear thinning behavior and viscoelastic moduli was analyzed. Its significance was also presented with respect to the printability aspect and the capability to maintain structural integrity in complex 3D geometries. A porous woodpile architecture was 3D printed, and its piezoresistive performance was analyzed. This study demonstrates how tailored ink formulations can enable high-fidelity printing and enhance the sensor performance, highlighting the potential of DIW-printed MWCNT/PDMS composites for next-generation wearable electronics and soft robotic applications.

2 Materials and methods

2.1 Materials

Multi-walled carbon nanotubes (MWCNTs) (purity of $\geq$ 98%, diameters range 10–15 nm, and lengths 3–10 μm) were procured from Ultra Nanotech Pvt. Ltd, India. The polydimethylsiloxane (PDMS), comprising the base polymer and curing agent (Sylgard 184, Dow Corning), was sourced from Kevin Electrochem, India. Nanofibrillated cellulose (NFC) was procured from Aritech Chemazone Pvt. Ltd, India. Isopropyl alcohol (IPA) was used as the solvent and was supplied by Loba Chemie Pvt. Ltd, India. Polyethylene terephthalate (PET) sheets were procured from a local supplier.

2.2 Methods

2.2.1 Ink formulation. The conductive inks were formulated using MWCNTs as the active ingredient, PDMS as the polymer matrix, NFC as the dispersant, and IPA as the solvent. MWCNTs were selected as conductive fillers owing to their exceptional electrical conductivity, high thermal conductivity, superior tensile strength, and high aspect ratio.[33,34] PDMS was selected as the matrix material due to its mechanical flexibility, low cost, biocompatibility, and wide applicability in flexible electronics. Nanofibrillated cellulose (NFC) was incorporated as a bio-based dispersant to improve the dispersion stability and suppress MWCNT agglomeration, owing to its high aspect ratio, surface functionality, and fibrous network structure.[35] NFC outperforms other surfactants (e.g., Triton X-100 and sodium
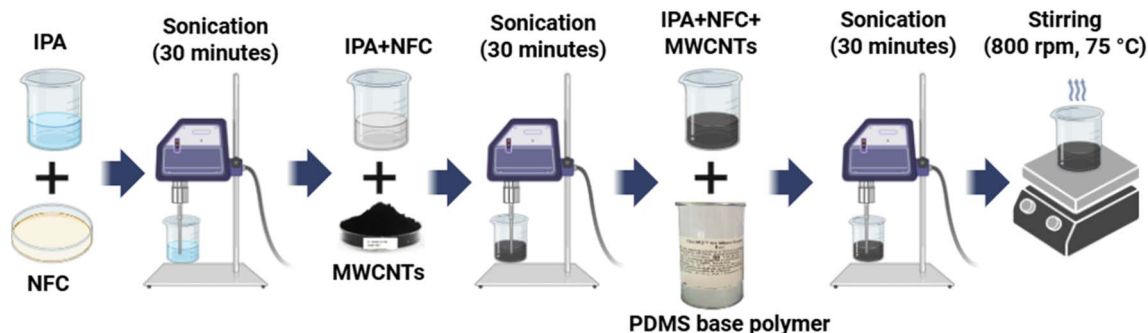
Fig. 1 Step-by-step schematic illustration for formulation of MWCNT/PDMS inks.

dodecyl sulfate) in dispersing MWCNTs, offering enhanced stability, electrical conductivity, and processability, thereby serving as a more effective and sustainable choice for conductive nanocomposite inks.[36,37] IPA was incorporated as the solvent due to its partial compatibility with both MWCNTs and PDMS, while also enhancing dispersion stability and ink printability.[38] Fig. 1 illustrates the MWCNT/PDMS ink formulation for DIW printing, wherein NFC was dispersed in IPA and sonicated for 30 min. Thereafter, the MWCNTs were mixed in the solution with a ratio of IPA : MWCNT of 50 : 1 and subjected to another sonication for 30 minutes. In the present study, sonication was carried out for only 30 min to maintain the integrity of the MWCNTs, as intense sonication can mechanically impact the MWCNTs by subjecting them to severe stress and heat, thus decreasing their length and considerably affecting their electrical conductivity.[39,40] The PDMS base polymer was added to the sonicated mixture (IPA + NFC + MWCNTs) and further sonicated for 30 min. To evaporate the IPA and to improve the mixing, the mixture was subjected to magnetic stirring at a temperature of 75 °C and 800 rpm. After complete evaporation of IPA, the curing agent was added to the mixture at a weight ratio of 1 : 10 to the base polymer and stirred manually before loading into the syringe barrel for printing. In this study, a series of conductive inks was prepared by varying the MWCNT concentration from 2 to 6 wt% and were designated as CNT-2, CNT-4, and CNT-6, corresponding to 2 wt%, 4 wt%, and 6 wt% MWCNT loadings, respectively. A fresh batch of ink was prepared for all the experiments using the same procedure to ensure consistency and assess reproducibility.

2.2.2 DIW printing. A syringe-based extrusion DIW setup was employed for the fabrication of 3D-printed structures using the formulated MWCNT/PDMS inks. Fig. 2 shows the DIW equipment, which consists of a computer-controlled three-axis motion stage integrated with an extrusion unit. The extrusion mechanism consists of a lead screw assembly coupled to an injection syringe. The 3D structures were designed using computer-aided design (CAD) *via* 3D modeling and then converted to G-code using Cura, an open-source program. The inks were dispensed into 10 mL syringes equipped with blunt-tip nozzles with an inner diameter of 600 μm. Subsequently, the syringes were installed on the three-axis motion stage and coupled to a motorized lead screw mechanism, which provided
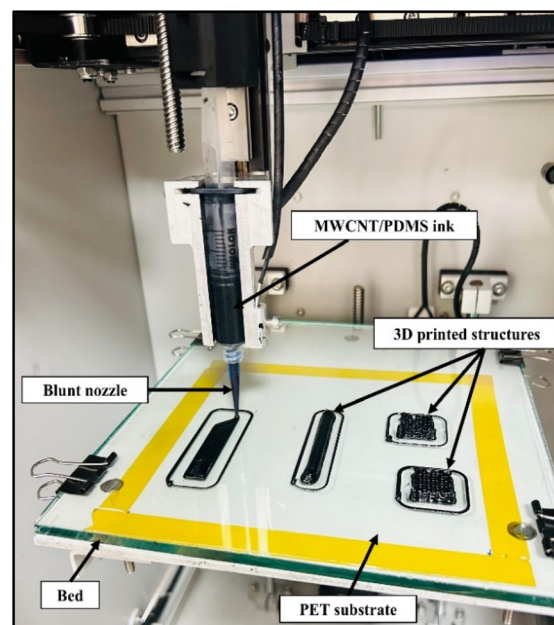

Fig. 2 Direct ink writing (DIW) setup.

the required pressure to drive the ink through the nozzle during the extrusion process. The porous woodpile structures were then fabricated by a layer-by-layer deposition technique on a PET substrate and cured at 80 °C for a duration of 2 hours.

2.2.3 Characterization. The rheological behavior of the formulated inks was evaluated at 25 °C using a rotational rheometer (RheolabQC, Anton Paar, Austria). Viscosity measurements were performed over a shear rate range of 1 to 100 s^{-1}, while the storage modulus (G') and loss modulus (G'') were determined through frequency sweep tests ranging from 0.1 to 100 rad s^{-1}. The morphological characteristics of the printed MWCNT/PDMS composite were examined using field emission scanning electron microscopy (FE-SEM; ZEISS Sigma 500 VP). Thermogravimetric analysis (TGA) was conducted using a PerkinElmer thermogravimetric analyzer at a heating rate of 10 °C min^{-1} over a temperature range of 25 °C to 800 °C. Mechanical characterization was conducted using a universal testing machine (UTM) (Tinius Olsen), while cyclic fatigue tests were performed on a servo-hydraulic UTM (BISS, India).
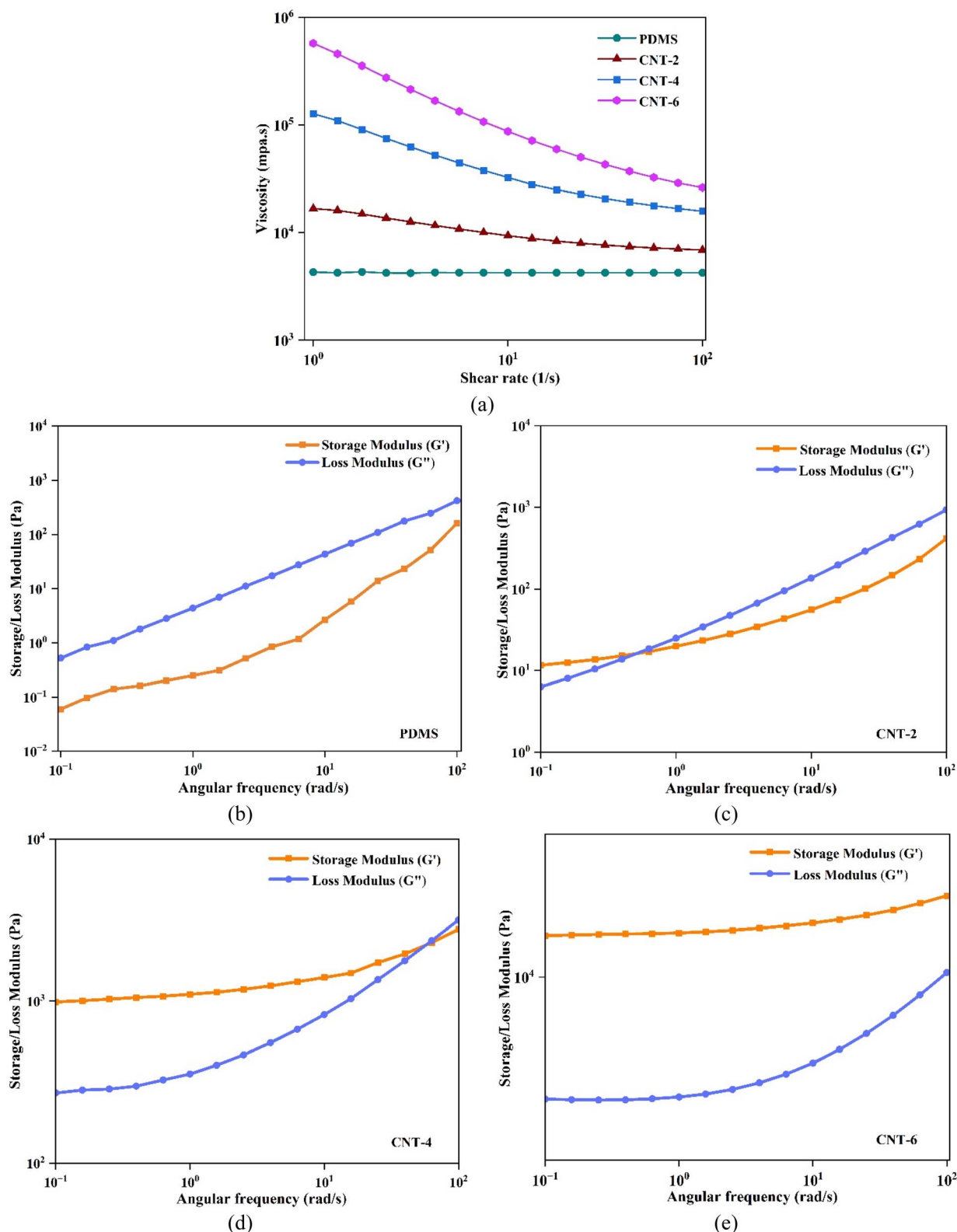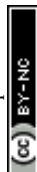
Fig. 3 (a) Apparent viscosity as a function of shear rate for MWCNT/PDMS inks having 0, 2, 4, and 6 wt% MWCNT. Storage modulus (G') and loss modulus (G'') as a function of angular frequency for (b) PDMS, (c) 2 wt%, (d) 4 wt%, and (e) 6 wt% MWCNTs formulations.

Electrical measurements were recorded using digital multi-meters (Keithley DMM6500 and UNI-T UT803).

3 Results and discussion

3.1 Rheological properties of the MWCNT/PDMS inks

A key factor in ensuring the printing of inks is the rheological optimization of MWCNT/PDMS inks, with viscosity being a crucial parameter for fine-tuning ink performance in the DIW process. For effective printing of inks into 3D structures, a printable DIW ink must satisfy the specified printing criteria, such as demonstrating shear thinning characteristics and possessing a storage modulus (G') greater than the loss modulus (G'').[41,42] Shear thinning refers to non-Newtonian behavior, where the ink's viscosity decreases with an increase in shear rate. The rheological characteristics of the inks were characterized by evaluating the change in viscosity as a function of the shear rate. The viscosity of the inks was altered by varying the MWCNT concentration from 2 to 6 wt%, and the results are presented in Fig. 3(a). From Fig. 3(a), it was observed that the pristine PDMS shows Newtonian fluid properties with relatively uniform viscosity and limited shear-thinning behavior, rendering it unsuitable for DIW applications. In contrast, the CNT-2 ink demonstrated slightly enhanced shear-thinning characteristics, although this was still insufficient for efficient printability. Both CNT-4 and CNT-6 inks exhibited pronounced shear-thinning behavior, confirming their suitability for the extrusion-based DIW process.

The Power Law model is a well-established approach for characterizing the flow behavior of non-Newtonian fluids, mathematically represented by the eqn (1).

$$\tau = K\dot{\gamma}^{n}, \tag{1}$$

where τ is the shear stress (Pa), $\dot{\gamma}$ is shear rate (s^{-1}), K is the flow consistency index, and n is the flow behavior or the Power law index.[43] The flow behavior is considered Newtonian when $n = 1$, $0 < n < 1$ corresponds to shear-thinning behavior; and $n > 1$ indicates shear-thickening. Also, as the power law index decreases, the degree of shear-thinning exhibited by the fluid increases. For pristine PDMS, the power law index n was calculated to be ≈ 1, confirming its behaviour as a Newtonian fluid, not suitable for the DIW printing. In contrast, the n values for the various MWCNT ink formulations were found to be less than 1, with values of 0.84, 0.65, and 0.43 corresponding to MWCNT concentrations of 2%, 4%, and 6% respectively. Table 1 details the results of rheological characterization and the printability aspect of the fabricated inks. The results indicate that increasing MWCNT content leads to more pronounced shear-thinning behavior, an essential characteristic of the ink for application in DIW.

For DIW inks, an appropriate yield stress is essential: it ensures the material can retain its printed shape under its own weight after the printing, while allowing continuous flow when the applied stress exceeds this threshold.[44] Generally, the optimal yield stress recommended range for DIW applications is ~100–1000 Pa.[45] In the study, the developed MWCNT/PDMS inks showed a clear trend of increasing yield stress with higher MWCNT loadings. Specifically, the CNT-2, CNT-4, and CNT-6 inks exhibited yield stress values of 12 Pa, 120 Pa, and 550 Pa, respectively (Table 1). This progressive increase indicates enhanced network formation and stronger interparticle interactions at higher CNT concentrations, which is desirable for stable and self-supporting structures during 3D printing. Notably, the CNT-2 ink's low yield stress suggests it may be more prone to slumping or spreading after extrusion, whereas CNT-4 and CNT-6 provide sufficient yield stress to retain printed geometries with good structural integrity. These results highlight the importance of tuning filler content to achieve optimal yield stress for DIW printing of inks.

In addition, oscillatory shear tests were conducted to evaluate the rheological behavior of the MWCNT/PDMS inks by determining the storage modulus (G') and loss modulus (G'') as a function of the angular frequency (Fig. 3(b)–(e)). The oscillatory results showed a clear transition from liquid-like to solid-like behavior with increasing MWCNT concentration in the PDMS matrix. Pristine PDMS exhibited a dominant viscous behavior ($G'' > G'$) across the frequency range, indicating a primarily fluid nature (Fig. 3(b)). The CNT-2 ink showed that a crossover point was observed at lower frequencies, indicating the formation of a weak bonding network. Also, $G'' > G'$ for a larger frequency domain, indicating a liquid behavior with limited ability to hold its shape after printing (Fig. 3(c)). For CNT-4, the crossover shifted to higher frequencies, suggesting the development of a stronger CNT network that sustains elasticity over a broader frequency domain. This transition, where G' consistently exceeds G'' across most of the tested domain, reflects a shift to dominant solid-like behavior, suitable for shape retention during and after extrusion (Fig. 3(d)). For CNT-6, no crossover point was detected within the measured range as G' remained consistently higher than G'' at all frequencies, signifying a well-percolated CNT network that provides robust structural integrity necessary for high-fidelity DIW printing (Fig. 3(e)). These results show that increasing the MWCNT content optimizes the balance between extrusion flow and post-

Table 1 Rheological and printability characteristics of PDMS and MWCNT/PDMS composites with varying MWCNT concentration

S. no.	MWCNT wt% in ink	Power law index (n)	Flow behavior classification	Yield stress (Pa)	Shape retention capability (Fig. 4)
1	PDMS (0 wt%)	≈ 1	Newtonian	0	Not printable
2	CNT-2 (2 wt%)	0.84	Shear-thinning (non-Newtonian)	12	Very poor
3	CNT-4 (4 wt%)	0.65	Shear-thinning (non-Newtonian)	120	Limited
4	CNT-6 (6 wt%)	0.43	Shear-thinning (non-Newtonian)	550	Optimal

deposition shape retention, with solid-like behavior becoming dominant beyond 4 wt% MWCNT.

3.2 DIW printing of porous woodpile structure

The structure of the pressure sensor enhances its sensitivity and stability of pressure sensor. Hence, this study used a porous woodpile structure to analyze the printability of the fabricated MWCNT/PDMS inks. Fig. 4(a) presents a schematic illustration of the porous woodpile structure obtained by DIW printing. All formulated MWCNT/PDMS inks were used to fabricate the porous woodpile structure using the DIW setup. The structure fabricated using CNT-2 ink resulted in ink spreading and poor shape fidelity (Fig. 4(b)). This was attributed to the insufficient viscosity and limited shear thinning behavior, which was also confirmed by rheological testing (Section 3.1).

In contrast, the CNT-4 ink demonstrated no ink spreading and offered improved structural definition and mechanical stability, attributed to its enhanced viscoelastic properties. However, it was still insufficient to fully preserve the geometric integrity of the porous woodpile architecture after 3D printing. The CNT-6 ink produced a well-defined and porous woodpile architecture (Fig. 4(d)), enabled by its improved rheological properties, including a dominant storage modulus and pronounced shear-thinning behavior, both of which are critical for maintaining structural fidelity during extrusion-based printing. The woodpile structure fabricated using the CNT-6 ink demonstrated exceptional mechanical flexibility, with no damage or structural degradation under bending, which can be attributed to the strong interfacial adhesion between the intersecting filaments, ensuring mechanical integrity and resilience under deformation (Fig. 4(e)). This highlights its potential for implementation in flexible and wearable pressure-sensing applications. A porous woodpile structure fabricated using the CNT-6 ink was subsequently employed for performance characterization as a flexible pressure sensor.

3.3 Morphological analysis of MWCNTs and MWCNT/PDMS composite

The field emission scanning electron microscopy (FE-SEM) was used to examine the microstructure of MWCNTs and the MWCNT/PDMS composite fabricated using CNT-6 ink. Fig. 5(a) illustrates the entangled network structure of the MWCNTs, which arises from the strong van der Waals interactions acting at the nanoscale. The SEM image of the MWCNT/PDMS composite, shown in Fig. 5(b), reveals a conducting network produced by the MWCNTs with a high aspect ratio, which is successfully distributed throughout the PDMS matrix. The formation of such an interconnected nanotube network enhances not only the structural integrity but also the electrical conductivity of the material, making it suitable for applications in flexible electronics.

Further, SEM analysis confirms the successful fabrication of the woodpile structure using CNT-6 ink *via* DIW. As shown in Fig. 5(c), the structure exhibits a well-aligned, multilayered architecture with excellent filament shape retention and consistent interlayer spacing. Fig. 5(d) presents the cross-sectional view, where the filaments maintain a nearly circular geometry with pore sizes of approximately 609.1 μm and 610.4 μm, indicating uniform deposition. These observations validate the rheological suitability of the CNT-6 ink for DIW and highlight the potential of the DIW for fabricating high-fidelity, porous architectures tailored for flexible and functional electronic applications.
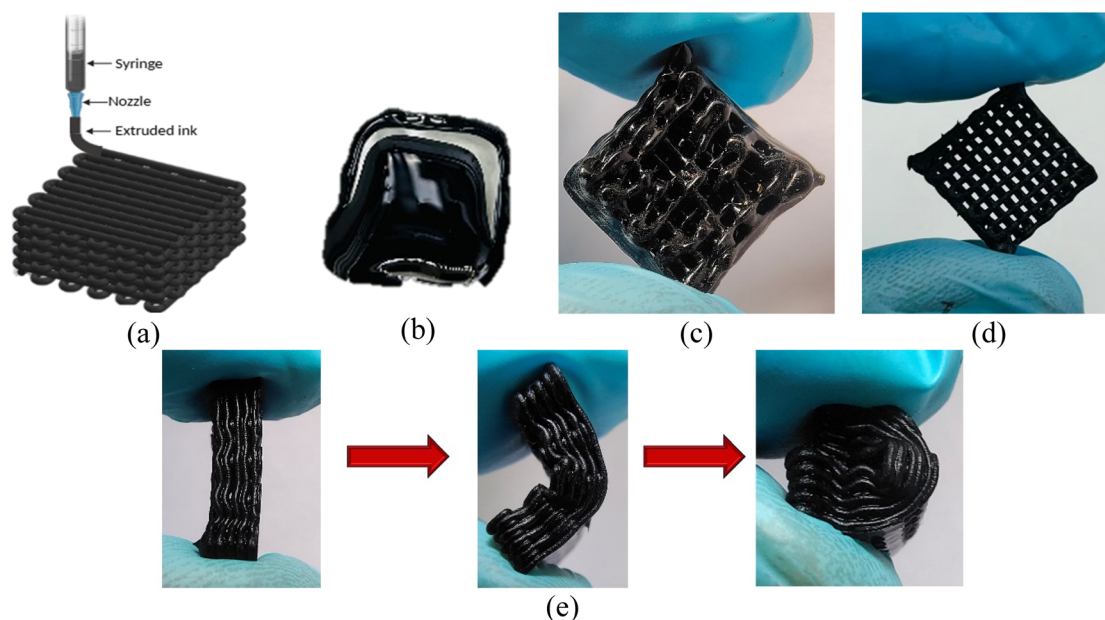

Fig. 4 (a) Illustration of the woodpile structure fabricated *via* direct ink writing (DIW). Woodpile structures printed using (b) 2 wt% (CNT-2) ink, (c) 4 wt% (CNT-4) ink, (d) 6 wt% (CNT-6) ink, (e) demonstration of the flexibility of the porous woodpile structure printed using CNT-6 ink.
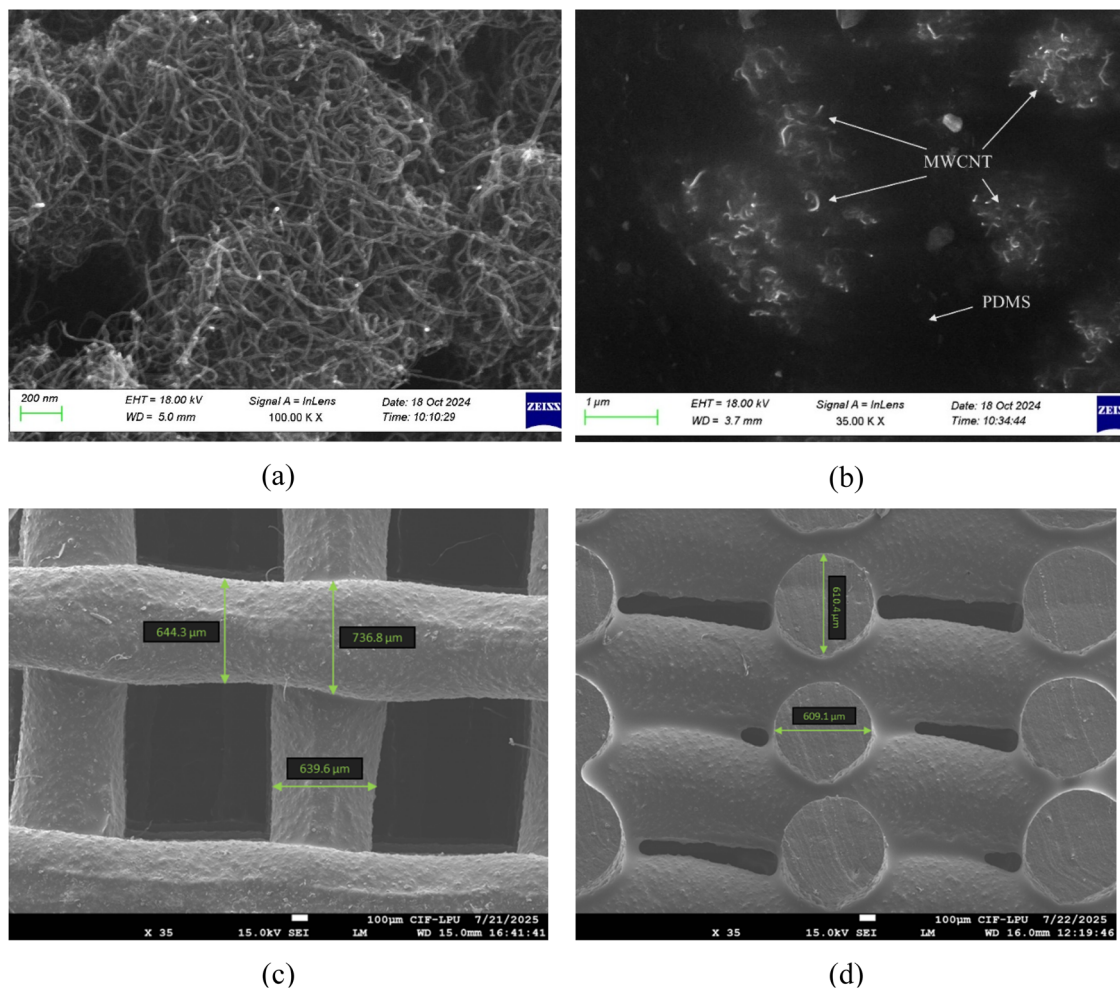
(a)

(b)

(c)

(d)

Fig. 5 SEM images representing (a) entangled network of pristine MWCNTs, (b) dispersion of MWCNTs within PDMS matrix, configuration of 3D printed woodpile structure (c) lateral and (d) cross-sectional view.
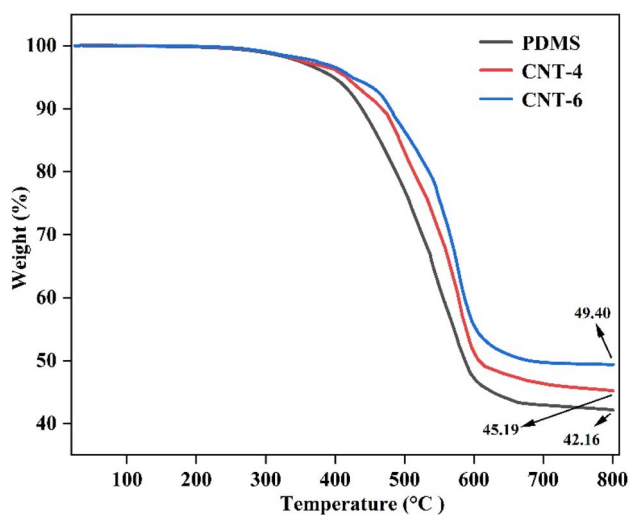
3.4 Thermal stability

Thermogravimetric analysis (TGA) was conducted to evaluate the thermal stability of the pristine PDMS and the MWCNT/PDMS composite fabricated with CNT-4 and CNT-6 inks. As shown in Fig. 6, the pristine PDMS exhibited an initial degradation temperature around 400 °C and a final mass residue of approximately 42.16 wt% at 800 °C. In contrast, the CNT-4 and CNT-6 composites demonstrated enhanced thermal stability, with higher onset degradation temperatures and increased residual masses of about 45.19 wt% and 49.40 wt% at 800 °C, respectively. The incorporation of MWCNTs significantly affects the thermal stability of the MWCNT/PDMS composite. The addition of MWCNTs resulted in a shift of the TGA curves towards higher temperatures, indicating enhanced thermal stability. This improvement is attributed to the uniform dispersion of MWCNTs within the PDMS matrix and the strong interfacial interactions between the nanotubes and the polymer chains, which together hinder the thermal degradation process.[46,47] These results confirm that the developed nanocomposite inks possess superior thermal stability, highlighting their potential for applications that demand elevated thermal endurance.

Fig. 6 TGA curves of pristine PDMS and MWCNT/PDMS composites for 4 wt% (CNT-4) and 6 wt% (CNT-6) inks.
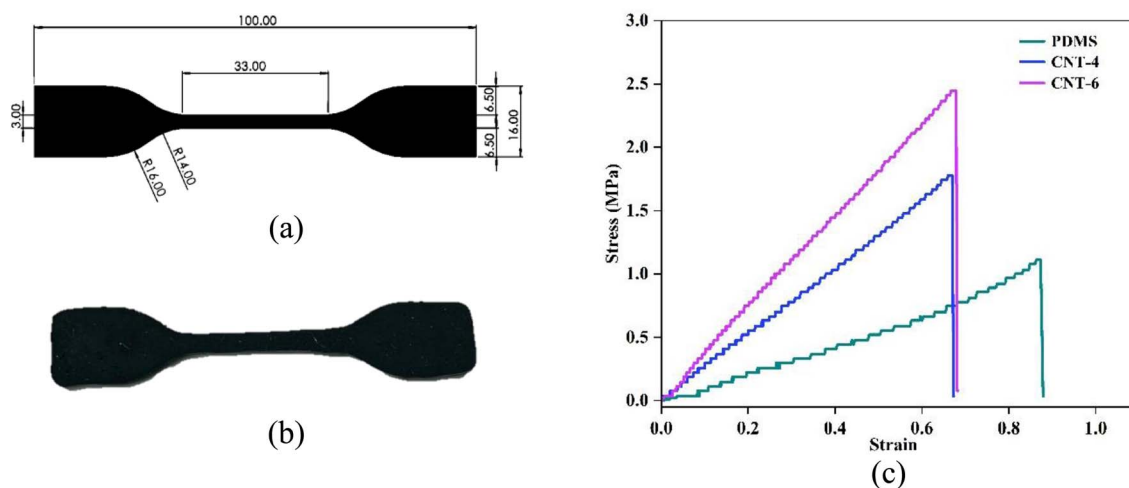
Fig. 7 (a) Dimensions of the tensile test specimen prepared in accordance with ASTM D412 standard, (b) 3D-printed tensile specimen fabricated using 6 wt% CNT (CNT-6) ink, (c) stress–strain curve for pristine PDMS and MWCNT/PDMS composites printed by 4 wt% (CNT-4) and 6 wt% (CNT-6) inks.

3.5 Mechanical properties of MWCNT/PDMS composites

The mechanical characteristics of the MWCNT/PDMS composites with varying MWCNT concentrations were examined to evaluate their strength and behavior under tensile loading conditions. Tensile tests were performed on a UTM equipped with a 10 kN load cell at a crosshead speed of 40 mm min^{-1}. For tensile testing, a dumbbell-shaped specimen was prepared in accordance with ASTM-D412, which specifies standard test methods for vulcanized rubber and thermoplastic elastomers.[48] Fig. 7(a) presents the geometry of the tensile specimen, whereas Fig. 7(b) displays the 3D-printed specimen fabricated using the CNT-6 ink. Owing to the inherent low viscosity and insufficient structural integrity of PDMS for direct 3D printing, tensile specimens were prepared by casting the material into a 3D-printed mold in accordance with the ASTM D412 standard. The tensile specimen with CNT-2 ink could not be fabricated by 3D printing because its low yield stress led to excessive spreading, rendering it unsuitable for DIW; hence, it was not considered. Fig. 7(c) presents the stress–strain curves of the cast PDMS specimen and 3D-printed specimens fabricated using the CNT-4 and CNT-6 inks. As observed from the stress–strain curves (Fig. 7(c)), a linear relationship between the stress and strain was maintained across varying MWCNT concentrations. The pristine PDMS sample fractured at a relatively low stress of 1.11 MPa with a strain of 0.87, whereas the 6 wt% MWCNT/PDMS composite exhibited significantly higher fracture stress

of 2.44 MPa with a strain of 0.68, highlighting the substantial reinforcement provided by the MWCNT incorporation.

The slope of the stress–strain curve corresponds to the Young's modulus of the composites. The Young's modulus of pristine PDMS was measured at 1.21 MPa, while the 6 wt% MWCNT/PDMS composite exhibited a modulus of 3.61 MPa, representing an approximately threefold increase. This enhancement is attributed to efficient stress transfer at the nanotube–matrix interface and the stiffening effect imparted by the MWCNTs, whose superior mechanical properties (Young's modulus ∼1 TPa and tensile strength ∼30 GPa) far exceed those of PDMS.[49] The tensile strength of the composites exhibited a trend similar to that of Young's modulus (Table 2).

3.6 Fatigue behavior of MWCNT/PDMS composite

The fatigue behavior of MWCNT/PDMS composites by CNT-6 ink was evaluated under tensile cyclic loading and unloading at varying strain amplitudes (10%, 20%, 30%, and 40%) to evaluate their mechanical durability and energy dissipation characteristics under repeated loading. As shown in the stress–strain hysteresis loops (Fig. 8(a)), the composites exhibited viscoelastic behavior with increasing energy dissipation at higher strain levels, as evidenced by the broadening of the loops. At lower strains (10% and 20%), the loops remained narrow and stable, indicating minimal stress softening and good structural integrity. In contrast, higher strain amplitudes (30% and 40%) led to increased hysteresis and more pronounced stress relaxation, suggesting enhanced polymer chain mobility and interfacial debonding between MWCNTs and the PDMS matrix. The evolution of maximum stress over 1000 cycles (Fig. 8(b)) revealed a gradual decline across all strain levels, with more significant degradation observed at higher strains of 30% and 40%. This stress-softening behavior is attributed to the Mullins effect,[50] which results from irreversible changes in the microstructure and weakening of the filler–matrix interface during the initial loading cycles. Despite this,

Table 2 Mechanical properties of pristine PDMS and MWCNT/PDMS composites at varying MWCNT loadings as determined from tensile testing

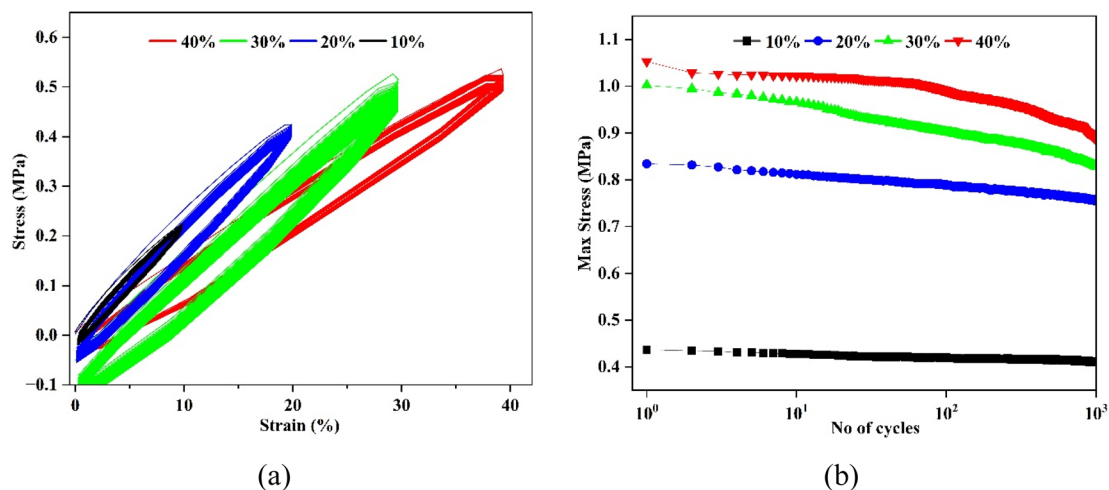| S. no.	MWCNT content (wt%)	Young's modulus (MPa)	Tensile strength (MPa)
1	Pristine PDMS	1.21	1.11
2	4 wt% (CNT-4)	2.62	1.78
3	6 wt% (CNT-6)	3.61	2.44

Fig. 8 (a) Cyclic stress–strain response of MWCNT/PDMS composites fabricated with CNT-6 ink at different strain levels, (b) variation of maximum stress with number of loading cycles under different strain conditions.

the composite maintained mechanical stability over multiple cycles, particularly at lower strains, underscoring its potential for applications in flexible and stretchable electronics. These results highlight the material's suitability for use in flexible pressure sensors, where reliable mechanical response and fatigue resistance under repeated deformation are essential.

3.7 Electromechanical characterization of MWCNT/PDMS flexible pressure sensor

The MWCNT particles establish conductive pathways within the matrix, forming a network of resistors.[51] The distribution of these particle connections is influenced by the external pressure, resulting in variations in resistance. Owing to the pressure caused by loading, the conductive networks experienced a process of disintegration and the development of percolation
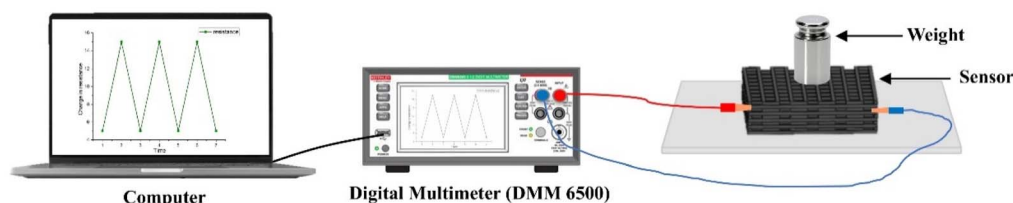

Fig. 9 Schematic representation of the experimental setup used for resistance measurements of the 3D-printed pressure sensor under applied load.
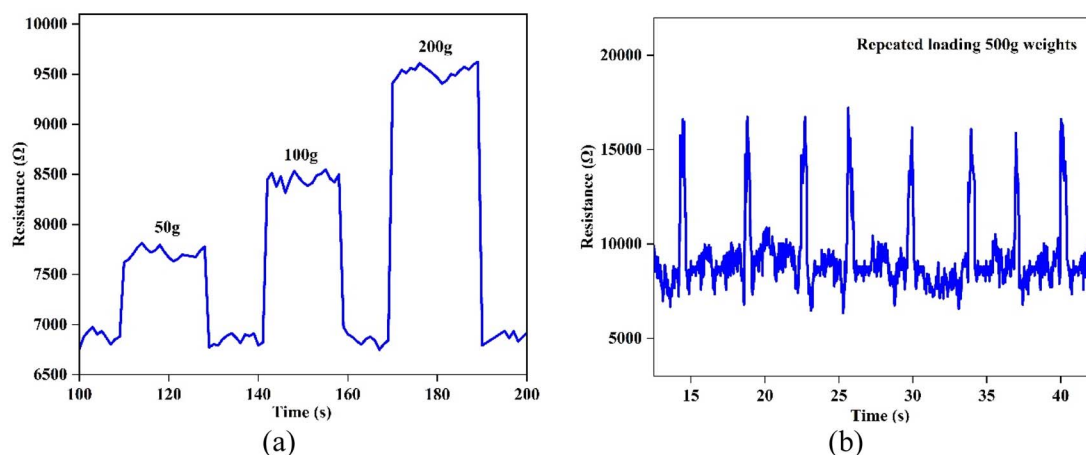

Fig. 10 Resistance response of the 3D printed woodpile structured flexible pressure sensor under (a) incremental static loads (50 g, 100 g, and 200 g), and (b) repeated cyclic loading at 500 g.

channels inside the particle network. Deformation of the MWCNT polymer nanocomposite induced alterations in the conductive pathways. Consequently, the electrical resistivity of the material may either increase or decrease. This behavior is correlated with the aspect ratio of the filler particles. Low-aspect-ratio fillers, such as carbon black, decrease resistance under external pressure, known as the negative pressure coefficient of resistance (NPCR). Conversely, resistance increases under pressure with high-aspect-ratio particles, such as CNTs, resulting in a positive pressure coefficient of resistance (PPCR) effect.[52] The PPCR effect in CNT/polymer composites describes the increase in electrical resistance under applied mechanical

pressure. This arises from the disruption of conductive pathways as pressure induces deformation of the polymer matrix, leading to increased inter-tube spacing and reduced electron tunneling between adjacent CNTs.[53] The effect is especially pronounced near the electrical percolation threshold, where minor structural changes significantly alter conductivity. In this study, the resistance increased with pressure and exhibited piezoresistive behavior. To assess the performance of the flexible pressure sensor, the 3D-printed sensor was placed on a flat surface. The ends of the flexible pressure sensor were connected to a digital multimeter (DMM6500, Keithley) using electrical wires and metallic clips. The multimeter was subsequently
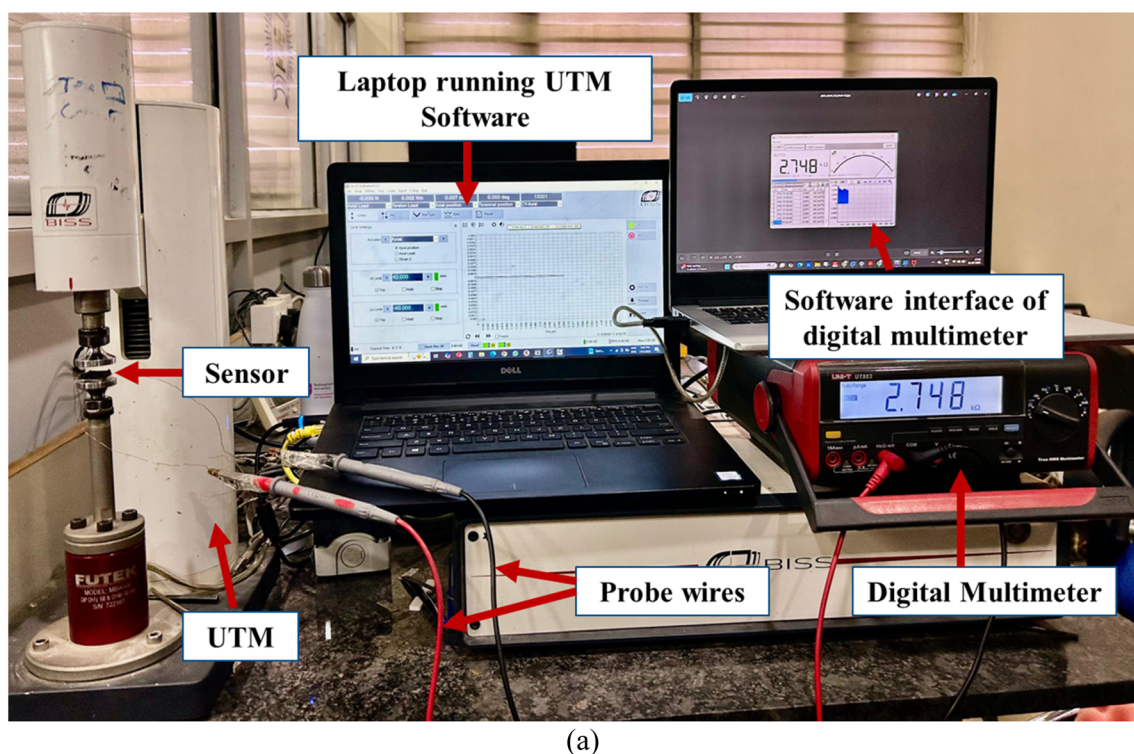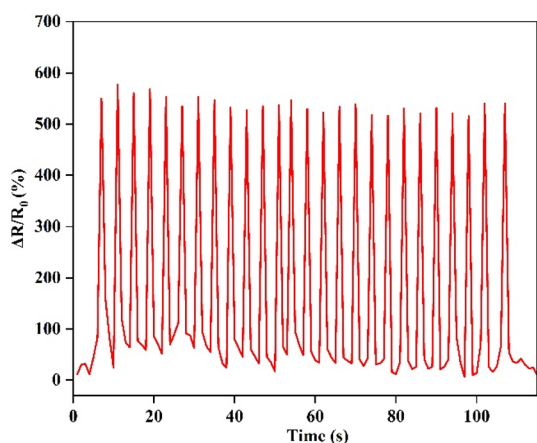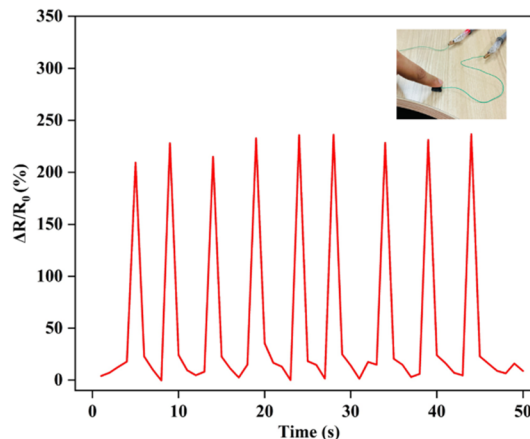
Fig. 11 (a) Experimental setup for electromechanical testing using a universal testing machine (UTM) coupled with resistance measurement *via* a digital multimeter, (b) relative resistance change ($\Delta R/R_0$) response under cyclic compression; (c) relative resistance change ($\Delta R/R_0$) response under repeated finger pressing (ΔR represents the change in electrical resistance during testing, and R_0 denotes the initial resistance of the sensor prior to loading).

Table 3 Comparison of MWCNT-based flexible pressure sensors reported in the literature and the present work

Study	Fabrication method	Sensing material	Sensitivity	Range (kPa)
Cai et al.[54]	Dip coating	MWCNTs/polyurethane (PU)	0.00125 kPa^{-1}	0–200
Zhong et al.[55]	Solution mixing	MWCNT/PDMS	0.004 kPa^{-1}	0–100
Zhou et al.[56]	Dip coating	CNTs/polyvinyl alcohol/polyvinylidene fluoride	0.0196 kPa^{-1}	0–40
He et al.[57]	Solution mixing	Modified-MWCNTs/PU	0.042 kPa^{-1}	0–63
Shao et al.[58]	Digital light processing	CNTs/PEDOT : PSS/PU dispersion	0.00354 S kPa^{-1}	0–22
Yang et al.[59]	Fused deposition modeling	CNT/Thermoplastic polyurethane	0.040 kPa^{-1}	0–20
This work	**DIW printing**	**MWCNTs/PDMS**	**0.047 kPa^{-1}**	**0–200**

interfaced with a computer *via* a USB connection, as shown in Fig. 9.

The piezoresistive performance of the porous woodpile pressure sensor was systematically evaluated under mechanical loading conditions to determine its sensitivity and stability. Under incremental static loads of 50 g, 100 g, and 200 g (Fig. 10(a)), the sensor exhibited a distinct and repeatable increase in resistance, indicating its sensitivity to the applied pressure. Resistance increased proportionally with applied load, confirming the deformation-induced compressive disruption of conductive pathways within the MWCNT/PDMS composite network. This behavior highlights the effective transduction of mechanical stimuli into electrical signals. Under dynamic conditions, as shown in Fig. 10(b), the sensor was subjected to repeated loading with a 500 g weight. The resistance response exhibited sharp and consistent peaks for each loading cycle, demonstrating excellent repeatability and fast response. These results confirm that the sensor delivers a reliable and stable performance under both static and dynamic loading conditions, making it a promising candidate for flexible and wearable piezoresistive sensing applications.

To assess the mechanical durability and pressure-sensing capability of the fabricated MWCNT/PDMS-based flexible pressure sensor, cyclic compressive loading–unloading tests were performed using a UTM equipped with a FUTEK load cell, as illustrated in Fig. 11(a). The sensor was positioned between the compression plates, and a controlled sinusoidal compressive force was repeatedly applied to simulate dynamic mechanical input. Force control and test execution were managed *via* the BISS testware software, while the real-time electrical response (resistance change) was continuously monitored using a UNI-T UT803 digital multimeter connected to a secondary laptop. Stable electrical connections were maintained using probe wires, ensuring accurate resistance measurements during each loading cycle. As shown in Fig. 11(b), the sensor exhibited repeatable and consistent relative resistance changes ($\Delta R/R_0$) under cyclic mechanical stress, confirming its high mechanical resilience and reliable electromechanical performance. Notably, the sensor maintained its electrical stability even after repeated cyclic loading, indicating minimal degradation in conductivity and sensing functionality. These findings highlight the suitability of the MWCNT/PDMS composite sensor for flexible and wearable electronics applications.

To further assess the sensor's applicability for human-interactive wearable electronics, a finger compression test was performed by manually applying pressure to the sensor surface, as illustrated in the inset of Fig. 11(c). The sensor demonstrated a clear, rapid, and repeatable response to finger-induced pressure, with ($\Delta R/R_0$) reaching up to ~200%, validating its capability to detect low-force stimuli. This confirms the sensor's potential for real-life applications in flexible electronics, such as tactile sensing, health monitoring, soft robotics, and human–machine interfaces.

The sensitivity of a pressure sensor is a critical parameter that quantifies its ability to convert mechanical stimuli into electrical signals. It is commonly defined as the ratio of the sensor's output response to the applied input pressure. For piezoresistive sensors, this is typically expressed as the normalized change in resistance with respect to applied pressure, mathematically given by eqn (2)

$$S = \frac{\Delta R/R_0}{P}, \qquad (2)$$

where S is the sensitivity, ΔR is the change in resistance, R_0 is the initial resistance, and P is the applied pressure. Based on this relationship, the fabricated flexible pressure sensor exhibited a sensitivity of 0.047 kPa^{-1}. Table 3 summarizes MWCNT-based flexible pressure sensors fabricated by different methods reported in the literature. The proposed DIW-printed MWCNT/PDMS sensor achieves a sensitivity of 0.047 kPa^{-1} over a broad sensing range of 0–200 kPa, exceeding the range of most reported studies and showing good sensitivity. This enhanced sensitivity demonstrates a high responsiveness to low-pressure stimuli and further supports its potential for precision pressure monitoring in flexible and wearable sensing applications.

4 Conclusions

In this study, 3D-printable conductive inks incorporating varying concentrations of MWCNTs were developed for the fabrication of flexible piezoresistive pressure sensors using DIW. Rheological analysis revealed that MWCNT loading above 4 wt% imparts the shear-thinning and solid-like viscoelastic properties necessary for successful DIW printing. Although both the CNT-4 and CNT-6 inks fulfilled the rheological criteria for extrusion and shape fidelity, only the CNT-6 formulation maintained the structural integrity of the complex woodpile architecture post-printing. Morphological analysis further confirmed the uniform distribution of the MWCNTs within the 3D-printed MWCNT/PDMS composites. The incorporation of MWCNTs into PDMS significantly enhanced the mechanical

properties of the composites, with the 6 wt% MWCNT/PDMS exhibiting a threefold increase in Young's modulus (3.61 MPa) and a higher tensile strength (2.44 MPa) than pristine PDMS, which is attributed to the effective stress transfer and superior mechanical properties of the MWCNTs. Furthermore, fatigue analysis demonstrated stable mechanical performance of the DIW-printed MWCNT/PDMS composites under cyclic loading, affirming their suitability for long-term flexible pressure sensing. The MWCNT/PDMS porous woodpile pressure sensor exhibited a robust PPCR effect with a good sensitivity of 0.047 kPa^{-1}, having excellent repeatability and stability under diverse loading conditions, establishing its potential for precision pressure monitoring in flexible and wearable piezoresistive sensing applications. Future work will focus on enhancing the sensor's sensitivity and exploring its integration into diverse real-world applications. This work represents a valuable contribution that could open new avenues for research and applications, particularly in optimizing material development in diverse fields, including wearable electronics, prosthetics, and robotics. Future works may focus on harnessing the geometric tunability to design next-generation flexible pressure sensors with enhanced sensitivity, pressure range, and overall performance.

Conflicts of interest

The authors declare that there are no conflicts of interest relevant to this communication.

Nomenclature

DIW	Direct ink writing
MWCNTs	Multiwalled carbon nanotubes
PDMS	Polydimethylsiloxane
AM	Additive manufacturing
NFC	Nanofibrillated cellulose
IPA	Isopropyl alcohol
PET	Polyethylene terephthalate
CAD	Computer-aided design
TGA	Thermogravimetric analysis
FE-SEM	Field emission scanning electron microscopy
UTM	Universal testing machine
PPCR	Positive pressure coefficient of resistance
NPCR	Negative pressure coefficient of resistance
PU	Polyurethane

Data availability

Data will be made available on request.

Supplementary information is available. See DOI: **https://doi.org/10.1039/d5na00796h**.

Acknowledgements

References

1 O. F. Emon, F. Alkadi, D. G. Philip, D. Kim and K. Lee, *Addit. Manuf.*, 2019, **28**, 629–638.

2 K. Meng, X. Xiao, W. Wei, G. Chen, A. Nashalian, S. Shen, X. Xiao and J. Chen, *Adv. Mater.*, 2022, **34**, 2109357.

3 S. Seneviratne, Y. Hu, T. Nguyen, G. Lan, S. Khalifa, K. Thilakarathna, M. Hassan and A. Seneviratne, *IEEE Commun. Surv. Tutorials*, 2017, **19**, 2573–2620.

4 X. Liu, B. Cui, X. Wang, M. Zheng, Z. Bai, O. Yue, Y. Fei and H. Jiang, *Adv. Healthcare Mater.*, 2023, **12**, 2202971.

5 F. He, X. You, W. Wang, T. Bai, G. Xue and M. Ye, *Small Methods*, 2021, **5**, 2001041.

6 M. T. Vijjapu, S. Khan, S. H. Abdullah, M. Jose, J. Zikulnig, L. Rauter, L.-M. Faller and J. Kosel, in *2023 IEEE Applied Sensing Conference (APSCON), IEEE*, 2023, pp. 1–3.

7 Y. Huang, X. Fan, S. Chen and N. Zhao, *Adv. Funct. Mater.*, 2019, **29**, 1808509.

8 D. Maddipatla, B. B. Narakathu and M. Atashbar, *Biosensors*, 2020, **10**, 199.

9 T. Zhang, Z. Li, K. Li and X. Yang, *Adv. Mater. Technol.*, 2019, **4**, 1900679.

10 Z.-H. Tang, S.-S. Xue, Y.-Q. Li, Z.-C. Zhu, P. Huang and S.-Y. Fu, *ACS Appl. Mater. Interfaces*, 2021, **13**, 48009–48019.

11 Y. Pang, K. Zhang, Z. Yang, S. Jiang, Z. Ju, Y. Li, X. Wang, D. Wang, M. Jian, Y. Zhang, R. Liang, H. Tian, Y. Yang and T.-L. Ren, *ACS Nano*, 2018, **12**, 2346–2354.

12 X. Guo, W. Hong, Y. Zhao, T. Zhu, H. Li, G. Zheng, J. Wang, G. Tang, J. Cao, Y. Wang, J. Yang, H. Zhang, D. Zhou, R. Feng, D. Xu, Q. Hong and Y. Xu, *Composites, Part A*, 2022, **163**, 107240.

13 W. Li, X. Jin, X. Han, Y. Li, W. Wang, T. Lin and Z. Zhu, *ACS Appl. Mater. Interfaces*, 2021, **13**, 19211–19220.

14 R. Yang, Y. Chang, X. Yang, J. Dai, Y. Chen, W. Chang and W. Xiong, *Composites, Part B*, 2021, **217**, 108818.

15 J. Park, Y. Lee, J. Hong, M. Ha, Y.-D. Jung, H. Lim, S. Y. Kim and H. Ko, *ACS Nano*, 2014, **8**, 4689–4697.

16 A. K. Pal, A. K. Mohanty and M. Misra, *RSC Adv.*, 2021, **11**, 36398–36438.

17 T. D. Ngo, A. Kashani, G. Imbalzano, K. T. Q. Nguyen and D. Hui, *Composites, Part B*, 2018, **143**, 172–196.

18 T. Xia, R. Yu, J. Yuan, C. Yi, L. Ma, F. Liu and G. J. Cheng, *Adv. Mater. Technol.*, 2021, **6**, 2000984.

19 H. Lei, K. Cao, Y. Chen, Z. Liang, Z. Wen, L. Jiang and X. Sun, *Chem. Eng. J.*, 2022, **445**, 136821.

20 J. A. Lewis and G. M. Gratson, *Mater. Today*, 2004, **7**, 32–39.

21 S. K. Maurya and N. C. Kothiyal, *Eur. J. Environ. Civ. Eng.*, 2024, **28**, 859–875.

22 J. S. Sidhu, A. Misra and A. Bhardwaj, *J. Mater. Sci.: Mater. Electron.*, 2024, **35**, 1958.

23 Q. Chen, P. F. Cao and R. C. Advincula, *Adv. Funct. Mater.*, 2018, **28**, 1–9.

24 K. Li, H. Wei, W. Liu, H. Meng, P. Zhang and C. Yan, *Nanotechnology*, 2018, **29**, 185501.

25 V. Diaz Mena, X. X. F. S. Romate, D. M. Diaz, M. S. Martinez and A. U. Fernandez, *IEEE Sens. J.*, 2024, **24**, 16902–16911.

26 Q. Wang, Y. Zheng, L. Feng, C. Li, S. Jiang and Y. Shang, *Surf. Interfaces*, 2025, **56**, 105544.

27 I. Elizabeth, C. Athira, S. J. Paul and B. P. Singh, *Carbon Lett.*, 2024, **34**, 1187–1195.

28 N. Naeem, S. Butt, Sumayya, Z. Afzal, M. Waseem Akram, M. Irfan, M. Atiq Ur Rehman, A. H. Baluch, G. ur Rehman and M. U. Farooq, *RSC Adv.*, 2025, **15**, 569–578.

29 K. Singh, S. Sharma, M. Gupta and C. C. Tripathi, *Microelectron. Eng.*, 2021, **250**, 111631.

30 Y. Liu, J. Xu, Y. Li, Y. Nie, H. Kang and W. Han, *Nanoscale*, 2025, **17**, 18583–18592.

31 Y. Jin, S. Xue and Y. He, *Adv. Mater.*, 2025, **37**, 2500076.

32 W. Li, X. Liu, Y. Wang, L. Peng, X. Jin, Z. Jiang, Z. Guo, J. Chen and W. Wang, *Discover Nano*, 2024, **18**, 88.

33 J. DeGraff, R. Liang, M. Q. Le, J.-F. Capsal, F. Ganet and P.-J. Cottinet, *Mater. Des.*, 2017, **133**, 47–53.

34 N. H. Alamusi, H. Fukunaga, S. Atobe, Y. Liu and J. Li, *Sensors*, 2011, **11**, 10691–10723.

35 A. Skogberg, S. Siljander, A.-J. Mäki, M. Honkanen, A. Efimov, M. Hannula, P. Lahtinen, S. Tuukkanen, T. Björkqvist and P. Kallio, *Nanoscale*, 2022, **14**, 448–463.

36 S. Siljander, P. Keinänen, A. Räty, K. R. Ramakrishnan, S. Tuukkanen, V. Kunnari, A. Harlin, J. Vuorinen and M. Kanerva, *Int. J. Mol. Sci.*, 2018, **19**, 1–14.

37 H. Mohan, M. Bartkowski and S. Giordani, *Appl. Sci.*, 2021, **11**, 10565.

38 J. H. Kim, J. Y. Hwang, H. R. Hwang, H. S. Kim, J. H. Lee, J. W. Seo, U. S. Shin and S. H. Lee, *Sci. Rep.*, 2018, **8**, 1–11.

39 R. Sadri, G. Ahmadi, H. Togun, M. Dahari, S. N. Kazi, E. Sadeghinezhad and N. Zubir, *Nanoscale Res. Lett.*, 2014, **9**, 4–13.

40 M. Mohiuddin and S. Van Hoa, *Nanoscale Res. Lett.*, 2011, **6**, 1–5.

41 S. Guo, K. Qiu, F. Meng, S. H. Park and M. C. McAlpine, *Adv. Mater.*, 2017, **29**, 1701218.

42 Z. Tang, S. Jia, X. Shi, B. Li and C. Zhou, *Polymers*, 2019, **11**, 666.

43 Q. Zheng, B. Xie, Z. Xu and H. Wu, *Int. J. Extreme Manuf.*, 2023, **5**, 035002.

44 J. A. Lewis, *Adv. Funct. Mater.*, 2006, **16**, 2193–2204.

45 S. Tagliaferri, A. Panagiotopoulos and C. Mattevi, *Mater. Adv.*, 2021, **2**, 540–563.

46 S. Fu, Y. Wang, Y. Zhong, J. Deng, Z. Zhang, H. Zhao and T. Chen, *Polym. Adv. Technol.*, 2025, **35**, e6312.

47 J. Yan, B. Kim and Y. G. Jeong, *J. Mater. Sci.*, 2015, **50**, 5599–5608.

48 ASTM International, 2003, DOI: **10.1520/D0412-98AR02E01**.

49 H. I. Kim, M. Wang, S. K. Lee, J. Kang, J. Do Nam, L. Ci and J. Suhr, *Sci. Rep.*, 2017, **7**, 1–7.

50 S. Shajari, M. Mahmoodi, M. Rajabian, K. Karan, U. Sundararaj and L. J. Sudak, *Adv. Electron. Mater.*, 2020, **6**, 1–13.

51 L. Vaisman, H. D. Wagner and G. Marom, *Adv. Colloid Interface Sci.*, 2006, **128–130**, 37–46.

52 S. Stassi, V. Cauda, G. Canavese and C. Pirri, *Sensors*, 2014, **14**, 5296–5332.

53 Z. Wang and X. Ye, *Nanotechnology*, 2014, **25**, 285502.

54 Y. Cai, L. Liu, X. Meng, J. Wang, C. Zhang, J. Li, Z. Lu and J. A. Duan, *RSC Adv.*, 2022, **12**, 34117–34125.

55 H. Zhong, R. Fu, S. Chen, Z. Zhou, Y. Zhang, X. Yin and B. He, *Nanotechnology*, 2022, **33**, 345502.

56 Q. Zhou, T. Chen, S. Cao, X. Xia, Y. Bi and X. Xiao, *Appl. Phys. A: Mater. Sci. Process.*, 2021, **127**, 667.

57 Y. He, Y. Ming, W. Li, Y. Li, M. Wu, J. Song, X. Li and H. Liu, *Sensors*, 2018, **18**, 1338.

58 Y. Shao, Q. Zhang, Y. Zhao, X. Pang, M. Liu, D. Zhang and X. Liang, *Materials*, 2021, **14**, 27–32.

59 L. Yang, X. Liu, Y. Xiao, Y. Zhang, G. Zhang and Y. Wang, *Adv. Mater. Technol.*, 2023, **8**, 1–9.